

# Near-infrared spectroscopy of the adult head: effect of scattering and absorbing obstructions in the cerebrospinal fluid layer on light distribution in the tissue

Hamid Dehghani and David T. Delpy

Previous modeling of near-infrared (NIR) light distribution in models of the adult head incorporating a clear nonscattering cerebrospinal fluid (CSF) layer have shown the latter to have a profound effect on the resulting photon measurement density function (PMDF). In particular, the presence of the CSF limits the PMDF largely to the outer cortical gray matter with little signal contribution from the deeper white matter. In practice, the CSF is not a simple unobstructed clear layer but contains light-scattering membranes and is crossed by various blood vessels. Using a radiosity-diffusion finite-element model, we investigated the effect on the PMDF of introducing intrusions within the clear layer. The results show that the presence of such obstructions does not significantly increase the light penetration into the brain tissue, except immediately adjacent to the obstruction and that its presence also increases the light sampling of the adjacent skull tissues, which would lead to additional contamination of the NIR spectroscopy signal by the surface tissue layers. © 2000 Optical Society of America

OCIS codes: 300.6340, 170.3660.

## 1. Introduction

Near-infrared spectroscopy (NIRS) of the head, which was initially applied to the monitoring of changes in the oxygenation level of the neonatal brain,<sup>1,2</sup> is now increasingly being used to study the adult brain.<sup>3-5</sup> Its use involves the application of near-infrared (NIR) light to the surface of the head with an optical fiber and the collection of exiting light from a point on the same surface with a similar fiber. The separation of source-detector optodes is usually no less than 10 mm and no larger than 70 mm, with larger separation providing information from deeper tissue. Changes of optical attenuation are measured over a period of time over a number of wavelengths, and these can be related to changes in hemoglobin and cytochrome oxidase concentrations within the area under investigation.<sup>6</sup>

Until recently, most interpretations of results were based on the single assumption that the area under

investigation is homogeneous and single layered. This assumption in reality is not correct, since the light traveling from the source to the detector will travel through at least five different layers, namely, scalp and skull, cerebrospinal fluid (CSF), and gray and white matter. Each of these layers will contribute to the total path taken by the light, and its attenuation will obviously have an effect on the overall results. Of these layers, the most important is the CSF, because previous numerical modeling has shown that the path taken by the light is significantly influenced by its presence.<sup>7-12</sup>

It is clinically important to be able to measure with some accuracy the contribution of the absorption change *in the brain* to the detected signal and the volume of *brain* tissue interrogated. This will obviously be effected by the nonhomogeneous structure of the head and in particular the presence and geometry of the CSF layer. Present numerical analysis of photon migration within tissue is usually based on the diffusion approximation of the Boltzmann transport equation, and this is not valid where scatter is small or negligible as would be the case in the clear CSF. Alternative attempts to examine the effects of including clear layers in the head have relied on Monte Carlo models,<sup>7</sup> finite-difference transport models,<sup>13,14</sup> or a hybrid radiosity finite-element model.<sup>9</sup> However, all these models have the disadvantage of requiring considerable computation time. For the research pre-

---

The authors are with the Department of Medical Physics and Bioengineering, University College of London, London WC1E 6JA, United Kingdom. H. Dehghani's e-mail address is dehghani@medphys.ucl.ac.uk.

Received 11 January 2000; revised manuscript received 16 May 2000.

0003-6935/00/254721-09\$15.00/0

© 2000 Optical Society of America

sented here we used a new fast modeling method with a radiosity-diffusion-based finite-element model.<sup>11</sup>

In previous studies modeling the effect of the CSF layer it has been shown that the presence of this clear layer significantly reduced the penetration of light into the deeper underlying cortical white matter, with the *detected* light having largely been confined to the outer cortical gray matter and the inner skull tissue. Surprisingly, the presence of the CSF-filled voids penetrating the cortical surface and mimicking the presence of sulci on the brain surface have little effect on the overall light distribution.<sup>7</sup>

In the real head, however, the CSF layer is not an uninterrupted structure, and it contains light-scattering membranes (the arachnoid membranes) and is traversed by various blood vessels. It has been suggested that the presence of these light-scattering and light-absorbing structures within the CSF layer may result in significant alteration of the light distribution around this otherwise clear layer.

Our aim in this study was therefore to look *specifically* at the effects of these intrusions in the CSF on the light distribution and hence on the contribution of the various tissues in the adult head to the NIRS signal (the signal of interest here being the measured light *intensity*, the parameter most commonly measured by the existing commercially available NIRS instruments). To do this, we investigated the photon measurement density function (PMDF) within a series of models of the adult head containing a clear CSF ring. The PMDF defines the sensitivity of the measured data to a change in the optical parameter of interest (in this instance the absorption function) within a region or element. We investigated the nonsmoothness of the CSF layer within the head by introducing block intrusions within the smooth CSF layer and show the effects of both single and multiple obstructions in the CSF ring and the corresponding PMDF within the model.

## 2. Forward Model

### A. Three-Layer Diffusive Model

Under the assumption that scattering dominates absorption in a region of interest the Boltzmann transport equation can be simplified to the diffusion approximation that in the frequency domain is given by

$$-\nabla \cdot \kappa(\mathbf{r}) \nabla \Phi(\mathbf{r}, \omega) + \left( \mu_a + \frac{i\omega}{c} \right) \Phi(\mathbf{r}, \omega) = q_0(\mathbf{r}, \omega), \quad (1)$$

where  $q_0(\mathbf{r}, \omega)$  is an isotropic source and  $\Phi(\mathbf{r}, \omega)$  is the photon density at position  $\mathbf{r}$ . The diffusion coefficient  $\kappa$  is given by

$$\kappa = 1/3(\mu_a + \mu'_s). \quad (2)$$

Here  $\mu_a$  is the tissue absorption;  $\mu_s$  the tissue-scatter coefficient; and  $\mu'_s = \mu_s(1 - g)$ , the transport-scatter coefficient, where  $g$  is the mean cosine of the single-scatter function (the anisotropy factor). Theoretical

and experimental results have so far demonstrated the validity of these equations under appropriate conditions where  $\mu'_s \gg \mu_a$ .<sup>15-17</sup>

### B. Four-Layer Diffusive Model with a Void Layer

We have modeled a nonscattering region within a diffusing medium, using a new radiosity-diffusion model.<sup>11</sup> Within a clear nonscattering region, photon migration can be calculated with the radiosity theory.<sup>18</sup> This theory simply calculates the irradiance of a surface from a light source at a given point and angle. In the case of a clear layer with an absorption coefficient  $\mu_a$ , the irradiance at a point  $\mathbf{r}_2$  on a surface  $\Gamma_2$ , which is due to a source  $\mathbf{r}_1$  on another surface  $\Gamma_1$ , is given as

$$\Gamma_2^i(\mathbf{r}_2) = \frac{I_1(\mathbf{r}_1) \cos(\theta_1) \cos(\theta_2)}{|\mathbf{r}_1 - \mathbf{r}_2|^2} \exp[-|\mathbf{r}_1 - \mathbf{r}_2| \times (\mu_a + i\omega/c)], \quad (3)$$

where  $I_1$  is the source strength from point  $\mathbf{r}_1$  on surface  $\Gamma_1$ .  $|\mathbf{r}_1 - \mathbf{r}_2|$  represents the distance between the two points.  $\theta_1$  is the angle between the source vector from point  $\mathbf{r}_1$  and the normal at point  $\mathbf{r}_1$ , and  $\theta_2$  is the angle between the source vector at point  $\mathbf{r}_2$  and the normal at point  $\mathbf{r}_2$ .

This radiosity-diffusion method for calculating photon propagation in diffusing tissue containing nonscattering regions has shown good agreement with models of the Boltzmann transport equation and the Monte Carlo models as well as with measured data.<sup>9,11</sup>

### C. Calculation of the Photon Measurement Density Function

Following Ref. 19, we use a finite-element method as a general and flexible method for solving the forward problem in arbitrary geometries. As developed in Refs. 20 and 21, given a domain  $\Omega$ , bounded by  $\partial\Omega$ , Eq. (1) is expressed in the finite-element-method framework as

$$[\mathbf{K}(\kappa) + \mathbf{C}(\mu) + \zeta \mathbf{A} + i\omega \mathbf{B}] \Phi(\omega) = \mathbf{q}_0(\omega), \quad (4)$$

where  $\zeta$  is a constant dependent on the refractive-index mismatch at the tissue boundary and the system matrices  $\mathbf{K}$ ,  $\mathbf{C}$ ,  $\mathbf{A}$ , and  $\mathbf{B}$  have entries given by

$$K_{ij} = \int_{\Omega} \kappa(\mathbf{r}) \nabla u_i(\mathbf{r}) \cdot \nabla u_j(\mathbf{r}) d^n \mathbf{r}, \quad (5)$$

$$C_{ij} = \int_{\Omega} \mu_a(\mathbf{r}) u_i(\mathbf{r}) u_j(\mathbf{r}) d^n \mathbf{r}, \quad (6)$$

$$B_{ij} = \frac{1}{c} \int_{\Omega} u_i(\mathbf{r}) u_j(\mathbf{r}) d^n \mathbf{r}, \quad (7)$$

$$A_{ij} = \int_{\partial\Omega} u_i(\mathbf{r}) u_j(\mathbf{r}) d^{n-1} \mathbf{r}, \quad (8)$$

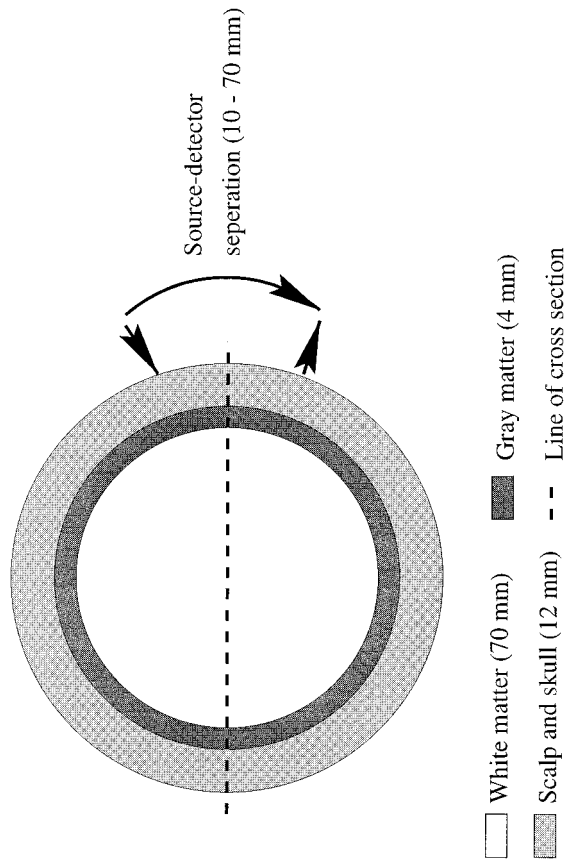


Fig. 1. Smooth-surfaced three-layer model. The model has a radius of 86 mm. The outer layer (representing scalp and skull) has a thickness of 12 mm; the middle layer (representing gray matter), a thickness of 4 mm; and the inner region (representing white matter), a radius of 70 mm. The optical properties are as stated in Table 1.

where  $u_i$  is the shape function associated with node  $i$  of the finite-element-method mesh and  $\Phi(\omega)$  and  $\mathbf{q}_0(\omega)$  are vectors representing the field and the source, respectively, at the nodal points at the mesh.

The above mechanism is easily modified to the case in which the domain  $\Omega$  contains nonscattering void regions. The forward problem [Eq. (4)] has an additional coupling term added for each void to give

$$[\mathbf{K}(\kappa) + \mathbf{C}(\mu) + \zeta \mathbf{A} + i\omega \mathbf{B} - \mathbf{E}(\omega)]\Phi(\omega) = \mathbf{q}_0(\omega), \quad (9)$$

where the new term  $\mathbf{E}(\omega)$  is assembled from component matrices for each void region, with entries given by

$$E_{ij} = \zeta \int_{A_i} u_i(\mathbf{r}_1) \int_{A_j} u_j(\mathbf{r}_2) h(\mathbf{r}_1, \mathbf{r}_2) \frac{\cos(\theta_1) \cos(\theta_2)}{|\mathbf{r}_1 - \mathbf{r}_2|^2} \times \exp - [|\mathbf{r}_1 - \mathbf{r}_2|(\mu_a + i\omega/c)] d^{n-1}\mathbf{r}_2 d^{n-1}\mathbf{r}_1, \quad (10)$$

where  $h(\mathbf{r}_1, \mathbf{r}_2)$  is a binary function with value 1 if points  $\mathbf{r}_1$  and  $\mathbf{r}_2$  are mutually visible.

To calculate the PMDF, we used the same princi-

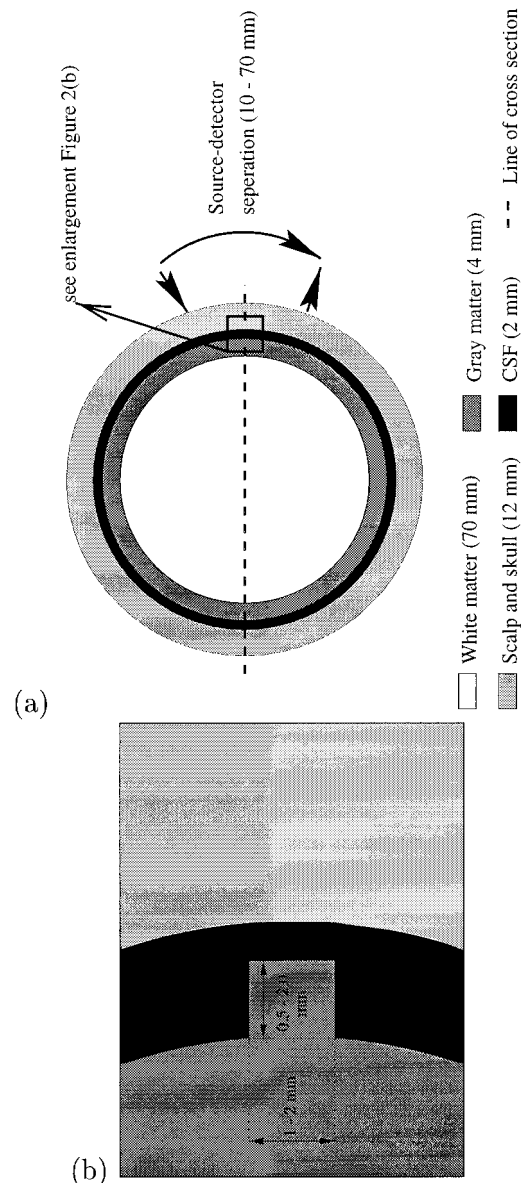


Fig. 2. (a) Smooth-surfaced four-layer model. The model has a radius of 86 mm. The outer layer (representing scalp and skull) has a thickness of 10 mm; the second layer (representing CSF), a thickness of 2 mm; the third layer (representing gray matter), a thickness of 4 mm; and the inner region (representing white matter), a radius of 70 mm. The optical properties are as stated in Table 1. (b) For the four-layer model with a single block intrusion the thickness of the block is either 1 or 2 mm, and its height is varied from 0.5 mm to 2.0 mm.

ples and methods as described above.<sup>19</sup> Let  $\Phi^i(\omega)$  be the solution vector in the mesh for a source at position  $i$  on the boundary, and let  $\Phi_{\text{Adj}}^j(\omega)$  be the solution vector in the mesh for an adjoint source at position  $j$  on the boundary. For integrated intensity, where the solutions are simply the Fourier-domain results at frequency zero, the reciprocity theorem states that for the absorption kernel we have

$$\text{PMDF}(i, j) = \Phi^i \times \Phi_{\text{Adj}}^j. \quad (11)$$

**Table 1. Definition of the Model Layers and Their Optical Properties**

Layer	$\mu'_s$ (mm <sup>-1</sup> )	$\mu_a$ (mm <sup>-1</sup> )
Scalp and skull	2.0	0.04
CSF	—	0.005
Gray matter	2.5	0.025
White matter	6.0	0.005

**3. Methods and Results**

The PMDF for the following models were calculated:

1. A three-layer model for which no CSF was taken into consideration. This consisted of an outer layer representing the scalp and skull combined, a gray-matter layer, and a white-matter layer. All layers were considered to have smooth boundaries (Fig. 1). Here the diffusion approximation alone is used to calculate the PMDF; therefore no CSF layer was included, since this approximation is not valid where there is no scatter or where the scatter is much smaller than absorption.

2. A four-layer model consisting of a scalp and skull, a CSF layer, a gray-matter layer, and a white-matter layer. All layers were considered to have smooth boundaries [Fig. 2(a)].

3. A four-layer model as in the previous case, except that the gray-matter layer included a single block intrusion into the CSF layer at a position located equidistant between the source and the detector. This single block was given the same optical parameters as the gray matter [Fig. 2(b)].

The optical properties of each layer are shown in Table 1. The exact characteristics of the models, including mesh sizes and the source model, are tabulated in Table 2.

The PMDF's for a single measurement type of intensity and six different source-detector separations (15, 10, 30, 40, 60, and 70 mm) were calculated for each model. For the model with a single block intrusion into the CSF layer the size of the block was varied between a height of 0.5–2.0 mm with a width of 1 mm. When the intrusion has a height of 2 mm, it completely extends from the gray matter to the inside of the skull layer and therefore fully blocks the CSF layer. The PMDF for a model for which the block has a height of 1.5 mm and a width of 2 mm was also calculated.

The calculated PMDF's for all models, for optode separations of 40, 50, and 70 mm, are shown in Fig. 3. From Fig. 3(a) it is seen that for the three-layer model for which no CSF layer is taken into consideration the well-known banana-shaped PMDF is obtained. It is also seen that, for increasing optode separation, the regions deeper within the white matter show great sensitivity to the measurement. In Fig. 3(b) the significant effect of the CSF layer can be seen in that the sensitive regions are more concentrated around the tissues immediately adjacent to the CSF layer. This effect arises because the attenuation suffered by photons that travel from source to detector by multiple diffuse reflections between the tissues on either side of the CSF layer is far less than for those that penetrate deeply into the scattering tissues.

When a single block intrusion is introduced into the CSF layer, it essentially blocks the path of the some photons propagating within the clear layer, the severity of its effect on light propagation depending on the size of the block. The results can be seen in Figs. 3(c)–3(g). When the block is small (height 0.5 mm and width 1 mm), the PMDF shows little change compared with the smooth CSF layer case. As the height of the block is increased no significant increase in the sensitivity of regions deeper within the white matter is seen. However, the block itself becomes highly sensitive, and regions directly below and above it also show more sensitivity. This is easily seen in the case with the 2-mm-high block. Here the block itself exhibits a high sensitivity, and the regions at either end of the block also show an increase in sensitivity compared with previous cases. The maximum increase in penetration depth is seen in the model where the block has a width of 2 mm. Here the wider block greatly reduces the number of photons traveling within the CSF layer and causes them to sample the scattering tissue on either side of the obstruction.

Figure 4 shows a cross section of the PMDF across the three-layer model in Fig. 3(a) for all source-detector spacings (the line corresponding to the cross section is shown in Fig. 1). These results show, as already known, that, as the optode spacing increases, the depth of penetration by the detected light also increases. For an optode spacing of 70 mm a region 35 mm deep (well into the white matter) shows good sensitivity to the measurement signal.

**Table 2. Definition of the Models**

Parameter	Three-Layer Model	Four-Layer Model
Scalp and skull	12 mm	10 mm
CSF	—	2 mm
Gray matter	4 mm	4 mm
White matter	70 mm	70 mm
Nodes	7051	9976
Elements	13829	18111
Source	Point at a depth of $1/\mu'_s$ mm	Point at a depth of $1/\mu'_s$ mm
Boundary condition	Robin	Robin

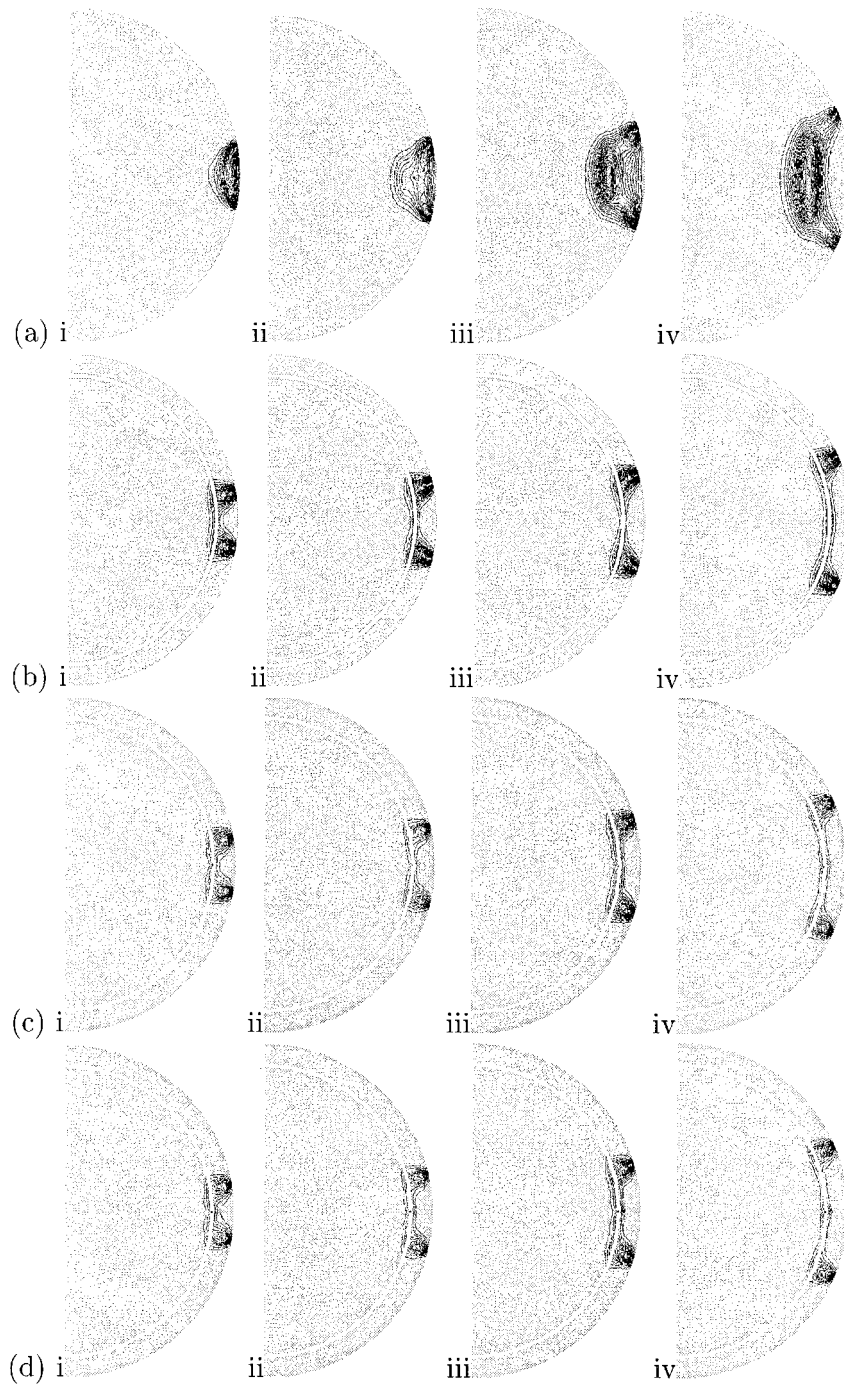


Fig. 3. Continues on next page.

Figure 5 shows a cross section of the PMDF across the smooth four-layer model in Fig. 3(b) for all source-detector spacings. The effects of the CSF layer can clearly be seen here as a significant reduction in the depth to which the light penetrates. For smaller optode spacings the effect is minimal as an optode separation of 10–15 mm; light penetration as far as the inner skull table is minimal. However, for optode spacings of more than 30 mm the effects are more substantial. For a separation of 30 mm the penetration depth along this midline profile is larger

than that at 40 and 50 mm. Also, at 30 mm the regions around the boundary of the CSF layer show a higher sensitivity than those of 40- and 50-mm spacings. This effect can be seen also in Fig. 3(b). For the 40- and 50-mm spacing the PMDF plots are seen to be stretched along the CSF boundary compared with those of the 30-mm spacing. It is not until the 70-mm optode spacing that slightly more penetration by the light is regained.

Figure 6 shows a cross section of the PMDF across all models including those with various sized block

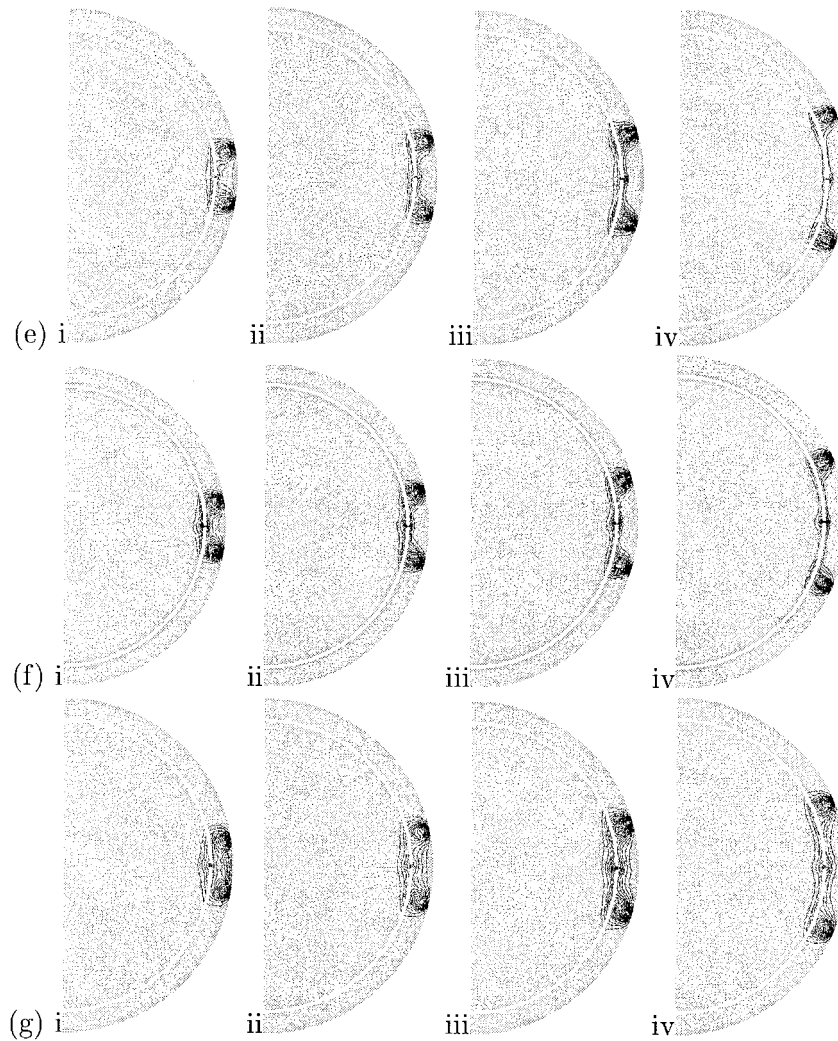


Fig. 3. PMDF for intensity data and absorption [units, optical density (OD) in millimeters]. (a) Three-layer model. (b) Four-layer model. (c) Four-layer model with block intrusion of width 1 mm and height 0.5 mm. (d) Four-layer model with block intrusion of width 1 mm and height 1 mm. (e) Four-layer model with block intrusion of width 1 mm and height 1.5 mm. (f) Four-layer model with block intrusion of width 1 mm and height 2 mm. (g) Four-layer model with block intrusion of width 2 mm and height 1.5 mm. The first column (i) shows the PMDF for a source-detector separation of 30 mm, the second (ii) for a separation of 40 mm, the third (iii) for a separation of 50 mm, and the fourth (iv) for a separation of 70 mm. For optical properties and model specifications see Tables 1 and 2. Each contour line represents a 5% change.

intrusions, for the optode spacing of 30 mm. Here minimum depth of penetration is obtained from the smooth four-layer model. An obvious feature from this plot is that, as soon as a CSF layer is introduced, the position of the peak sensitivity moves inward from the outer boundary of the model toward the CSF layer, and in fact this effect is not overcome until a large obstruction is introduced into the CSF. The maximum penetration is obtained when the obstruction is at its widest, since this allows for the interception of more photons as they travel through the CSF layer. The presence of a continuous obstruction extending from the gray matter to the skull (height of 2 mm) does not result in a greater penetration, but it provides greater sensitivity around the boundary of the CSF and within the obstruction itself.

Figure 7 shows a cross section of the PMDF across all models including those with various sized block intrusions, for the optode spacing of 40 mm. Here maximum penetration depth is obtained from the three-layer model where no CSF is present, whereas, again, the minimum depth is obtained from the smooth four-layer model. The maximum penetration is obtained from the use of the widest obstruction. The continuous obstruction from gray matter to the skull (height of 2 mm) again does not result in any greater penetration, but as seen above it provides greater sensitivity around the boundary of the CSF and within the obstruction itself. A similar pattern of results is seen in the PMDF's for the optode spacings of 50 and 70 mm (Figs. 8 and 9, respectively).

To see whether the attenuation of the obstruction would significantly change the light penetration

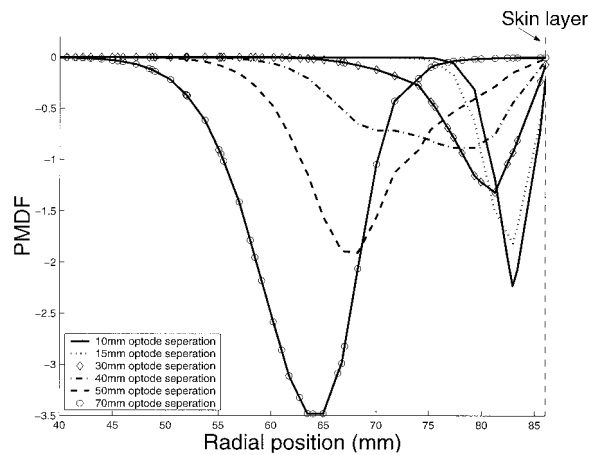


Fig. 4. PMDF for intensity data and absorption (units, OD in millimeters). Cross section through the three-layer model shown in Fig. 3(a). The dashed vertical line represents the boundary of the skin layer.

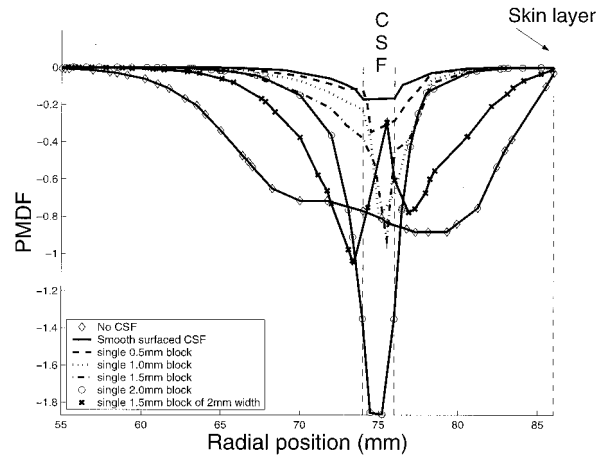


Fig. 7. PMDF for intensity data and absorption (units, OD in millimeters). Cross section through all models for a source-detector spacing of 40 mm. The dashed vertical lines represent the boundaries of the clear CSF layer and also the boundary of the skin layer.

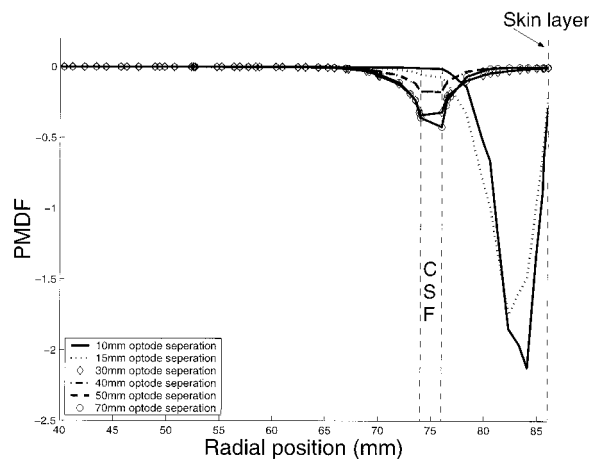


Fig. 5. PMDF for intensity data and absorption (units, OD in millimeters). Cross section through the smooth four-layer model shown in Fig. 3(b). The dashed vertical lines represent the boundaries of the clear CSF layer and also the boundary of the skin layer.

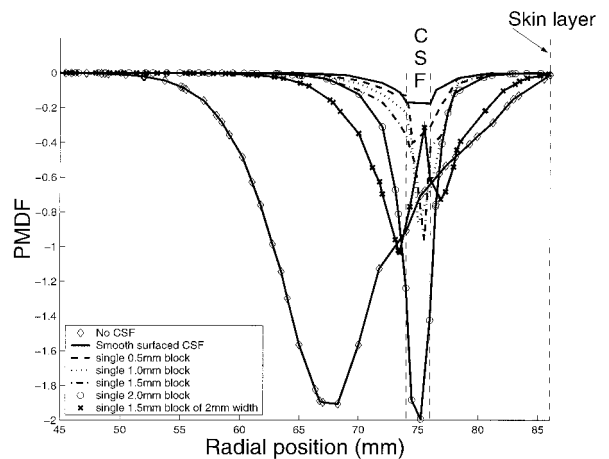


Fig. 8. PMDF for intensity data and absorption (units, OD in millimeters). Cross section through all models for a source-detector spacing of 50 mm. The dashed vertical lines represent the boundaries of the clear CSF layer and also the boundary of the skin layer.

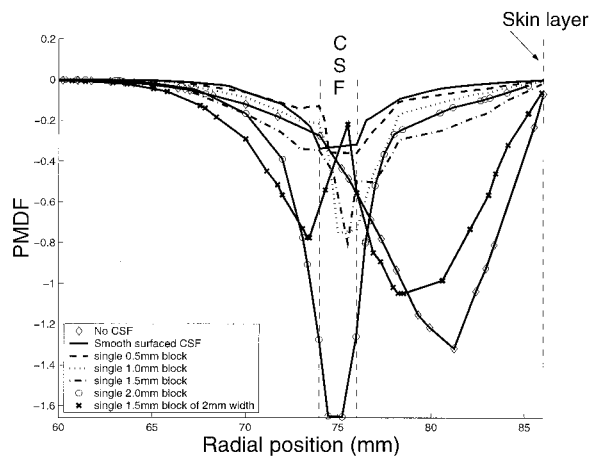


Fig. 6. PMDF for intensity data and absorption (units, OD in millimeters). Cross section through all models for a source-detector spacing of 30 mm. The dashed vertical lines represent the boundaries of the clear CSF layer and also the boundary of the skin layer.

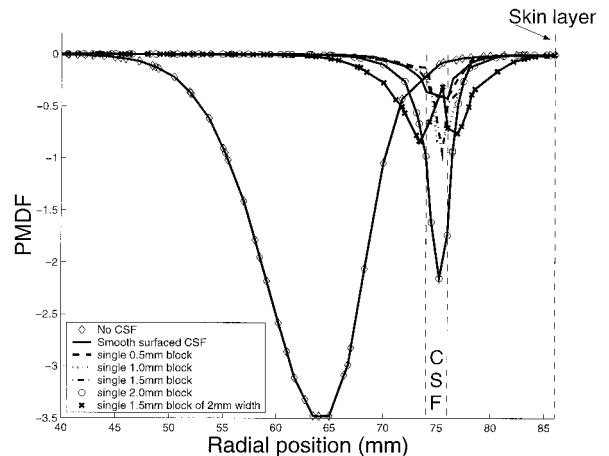


Fig. 9. PMDF for intensity data and absorption (units, OD in millimeters). Cross section through all models for a source-detector spacing of 70 mm. The dashed vertical lines represent the boundaries of the clear CSF layer and also the boundary of the skin layer.

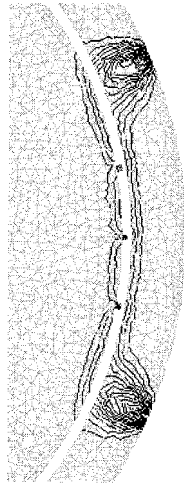


Fig. 10. PMDF for intensity data and absorption (units, OD in millimeters). The four-layer model [similar to Fig. 3(d) with three block intrusions of width 1 mm and height 1.0 mm and a source detector separation on 70 mm]. Each contour line represents a 5% change.

depth, the  $\mu_a$  of the block intrusion was increased to  $0.05 \text{ mm}^{-1}$  for all the above models and the PMDF's calculated again. This increase in the absorption of the block was found not to alter the PMDF's significantly, the results being similar to those obtained at the lower  $\mu_a$ .

Finally, the effects of including multiple intrusions were investigated (Fig. 10). Here three blocks of 1-mm width and 1-mm height were modeled at a distance of 12 mm apart. From the results it is seen that the area immediately adjacent to the block intrusions and the intrusions themselves again show enhanced sensitivity. However, these multiple obstructions do not result in a significant increase in light penetration into the cortical white matter in the model.

#### 4. Discussion and Conclusions

Various simple models of light propagation in the adult head have been investigated. The three-layer model with no CSF present confirmed previous observations that a reasonable sensitivity of the detected intensity to white matter can be obtained at larger optode spacing, but it is known that this three-layer model is not a good representation of the adult head. Therefore a four-layer model that includes a clear nonscattering layer has been used. This model confirmed that the presence of such a clear layer with smooth boundaries significantly reduces the penetration of light into the deeper tissues within the head, and therefore the sensitivity of the NIRS signal to changes within the white matter is reduced.

The effect of introducing intrusions within the CSF gap has been investigated. These intrusions were intended to mimic the nonsmoothness of the CSF layer within an adult head and the presence of light-scattering membranes and light-absorbing blood vessels on the surface of the gray matter. It has been

shown that, even with the introduction of intrusions that completely span the CSF layer, the sensitivity of the the NIRS signal to the deeper tissues is not greatly improved. However, the sensitivity of the signal to absorption changes in the intrusion itself is considerably increased together with that of the tissues immediately adjacent to the intrusion. This is because the light sampling of the adjacent tissue is increased, since the propagating photons have been forced to travel through the outer gray matter and the inner skull tissue to get around the obstruction.

For optode separations of less than 20–30 mm the effects of both the CSF and any intrusion are minimal, since at this separation the penetration of light into the cortical matter is small; but as the optode separation increases, the effects of the CSF become more significant. The depth at which the detected NIRS signals is most sensitive is greatly reduced because of the greatly reduced attenuation of light that travels from source to detector mainly within the CSF. Since the most common path for such photons will involve repeated diffuse scatters across the CSF layer, the NIRS is mainly sensitive to absorption changes that arise in the tissue immediately adjacent to the CSF layer. When an intrusion is placed within the CSF gap, it essentially blocks the path of some photons traveling through the CSF. Therefore the number of photons encountered by the intrusion is high, resulting in a high sensitivity of the NIRS signal to absorption changes in the intrusion itself and also in the regions immediately adjacent to it.

#### References

1. J. E. Brazy, D. V. Lewis, M. H. Mitnick, and F. F. Jobsis vander Vliet, "Noninvasive monitoring of cerebral oxygenation in pre-term infants: preliminary observations," *Pediatrics* **25**, 217–225 (1985).
2. J. S. Wyatt, D. T. Delpy, M. Cope, S. Wray, and E. O. R. Reynolds, "Quantification of cerebral oxygenation and haemodynamics in sick newborn infants by near infrared spectroscopy," *Lancet* **ii**, 1063–1066 (1986).
3. M. Ferrari, E. Zanette, I. Giannini, G. Sideri, C. Fieschi, and A. Carpi, "Effect of carotid artery compression test on regional cerebral blood volume, haemoglobin oxygen saturation and cytochrome-c-oxidase redox level in cerebrovascular patients," *Adv. Exp. Med. Biol.* **200**, 213–222 (1986).
4. N. B. Hampson, E. M. Camporesi, B. W. Stolp, R. E. Moon, J. E. Shook, J. A. Griebel, and C. A. Piantadosi, "Cerebral oxygen availability by NIR spectroscopy during transient hypoxia in humans," *J. Appl. Physiol.* **69**, 907–913 (1990).
5. Y. Hoshi and M. Tamura, "Detection of dynamic changes in cerebral oxygenation coupled to neuronal function during mental work in man," *Neurosci. Lett.* **150**, 5–8 (1993).
6. S. Wray, M. Cope, D. T. Delpy, J. S. Wyatt, and E. O. R. Reynolds, "Characterisation of the near infrared absorption spectra of cytochrome aa3 and haemoglobin for the non invasive monitoring of cerebral oxygenation," *Biochem. Biophys. Acta* **933**, 184–192 (1988).
7. E. Okada, M. Firbank, M. Schweiger, S. R. Arridge, M. Cope, and D. T. Delpy, "Theoretical and experimental investigation of near infrared light propagation in a model of the adult head," *Appl. Opt.* **36**, 21–31 (1997).
8. H. Liu, D. A. Boas, A. G. Yodh, and B. Chance "Influence of clear cerebrospinal fluid on NIR brain imaging and cerebral oxygenation monitoring," in *Advances in Optical Imaging and*

- Photon Migration*, R. R. Alfano and James G. Fujimoto, eds. Vol. 2 of OSA Trends in Optics and Photonics (Optical Society of America, Washington, D.C., 1996), pp. 372–375.
9. M. Firbank, S. R. Arridge, M. Schweiger, and D. T. Delpy, "An investigation of light transport through scattering bodies with non-scattering regions," *Phys. Med. Biol.* **41**, 767–783 (1996).
  10. A. H. Hielscher, R. E. Alcouffe, and R. L. Barbour, "Transport and diffusion calculations on MRI-generated data," in *Optical Tomography and Spectroscopy of Tissue: Theory, Instrumentation, Model, and Human Studies II*, B. Chance and R. R. Alfano, eds., Proc. SPIE **2979**, 500–508 (1997).
  11. S. R. Arridge, H. Dehghani, M. Schweiger, and E. Okada, "The finite element model for the propagation of light in scattering media: a direct method for domains with non-scattering regions," *Med. Phys.* **27**, 252–264 (2000).
  12. H. Dehghani, D. T. Delpy, and S. R. Arridge, "Photon migration in non-scattering tissue and the effects on image reconstruction," *Phys. Med. Biol.* **44**, 2897–2906 (1999).
  13. A. H. Hielscher, R. E. Alcouffe, and R. L. Barbour, "Comparison of finite-difference transport and diffusion calculations for photon migration in homogeneous and heterogeneous tissue," *Phys. Med. Biol.* **43**, 1285–1302 (1998).
  14. M. Firbank, E. Okada, and D. T. Delpy, "A theoretical study of the signal contribution of regions of the adult head to near infrared spectroscopy studies of visual evoked responses," *Neuroimag.* **8**, 69–78 (1998).
  15. R. A. J. Groenhuis, H. A. Ferwada, and J. J. Ten Bosch, "Scattering and absorption of turbid materials determined from reflection measurements. 1. Theory," *Appl. Opt.* **22**, 2456–2462 (1983); "Scattering and absorption of turbid materials determined from reflection measurements. 2. Measuring method and calibration," *Appl. Opt.* **22**, 2463–2467 (1983).
  16. T. Nakai, G. Nishimura, K. Yamamoto, and M. Tamura, "Expression of optical diffusion coefficient in high-absorption turbid media," *Phys. Med. Biol.* **42**, 2541–2549 (1997).
  17. M. Bassani, F. Martelli, G. Zaccanti, and D. Contini, "Independence of the diffusion coefficient from absorption: experimental and numerical evidence," *Opt. Lett.* **22**, 853–855 (1997).
  18. M. F. Cohen and J. R. Wallace, *Radiosity and Realistic Image Synthesis* (Academic, London, 1993).
  19. S. R. Arridge and M. Schweiger, "Photon-measurement density functions. II. Finite-element-method calculations," *Appl. Opt.* **34**, 8026–8037 (1995).
  20. S. R. Arridge, M. Schweiger, M. Hiraoka, and D. T. Delpy, "A finite element approach for modeling photon transport in tissue," *Med. Phys.* **20**, 299–309 (1993).
  21. M. Schweiger, S. R. Arridge, M. Hiraoka, and D. T. Delpy, "The finite element model for the propagation of light in scattering media: boundary and source conditions," *Med. Phys.* **22**, 1779–1792 (1995).